Tissue Elasticity Estimation with Optical Coherence Elastography: Toward Mechanical Characterization of *In Vivo* Soft Tissue

AHMAD S. KHALIL,[1] RAYMOND C. CHAN,[2] ALEXANDRA H. CHAU,[1,2] BRETT E. BOUMA,[2]
and MOHAMMAD R. KAAZEMPUR MOFRAD[3]

[1]Department of Mechanical Engineering, Massachusetts Institute of Technology, Cambridge, MA 02139; [2]Wellman Center for Photomedicine, Massachusetts General Hospital, Harvard Medical School, Boston, MA 02114; and [3]Department of Bioengineering, University of California, Berkeley, CA 94720

Abstract—High-resolution imaging provides a significant means for accurate material modulus estimation and mechanical characterization. Within the realm of *in vivo* soft tissue characterization, particularly on small biological length scales such as arterial atherosclerotic plaques, optical coherence tomography (OCT) offers a desirable imaging modality with higher spatial resolution and contrast of tissue as compared with intravascular ultrasound (IVUS). Based on recent advances in OCT imaging and elastography, we present a fully integrated system for tissue elasticity reconstruction, and assess the benefits of OCT on the distribution results of four representative tissue block models. We demonstrate accuracy, with displacement residuals on the order of 10^{-6} mm (more than 3 orders of magnitude less than average calculated displacements), and high-resolution estimates, with the ability to resolve inclusions of 0.15 mm diameter.

Keywords—Optical coherence tomography, Soft tissue, Elasticity estimation, FEM, Regularization.

INTRODUCTION

Elasticity estimation is best summarized as the effort to replace qualitative measures of elasticity with quantitative diagnostic tools. For many specimens, this is challenging because of their inhomogeneous field data and unique boundary conditions. The properties of biomaterials, for instance, often rely on complete measurements of important field information (i.e., displacement, stress, or strain). Researchers have modeled a variety of biological tissues in attempts to describe their mechanical behavior,[7,20,21] yet knowledge of soft tissue material properties remains limited.[23] This is partly due to the substantial sensitivity of elasticity values to particular specimens and testing setups and to the enormous elastic variability and heterogeneity of soft tissues—the elastic modulus of soft tissues spans 4 orders of magnitude.[12] A better understanding of soft tissue elasticity, and a system for accurately and efficiently predicting it, is therefore needed.

Imaging limitations and modality-specific differences also make tissue elasticity reconstruction a challenge. Since ultrasound-based tissue elastography for biomechanical strain imaging was first developed,[22] researchers have extended this technique to other imaging modalities, in hopes of generating more accurate strain maps for their specific problems. In intravascular ultrasound (IVUS) considerable effort has been invested in coronary arterial elastography[9,11,26] and today, IVUS elastography is the only method clinically demonstrated for strain characterization in coronary lesions. IVUS elastography is, however, limited to a spatial resolution of 200 μm for radial strain (oriented along each A-line). This limitation strongly impacts the characterization of potentially vulnerable lesions with fibrous caps smaller than 200 μm. Intravascular optical coherence tomography (OCT), an optical analog to IVUS, overcomes this limitation and offers significantly higher soft tissue contrast, overcoming the other major IVUS limitation: low contrast between different tissues.[18] Higher spatial resolution offers greater sensitivity to smaller tissue displacements, contributing to (i) the ability to resolve material properties of small-scale biological structures, such as the thin plaque cap, and (ii) the ability to obtain more data points for each unknown tissue sample to be characterized. Enhanced soft tissue contrast is beneficial in accurately visualizing internal plaque morphology and in potentially obtaining better prior information about tissue type. The sacrifice associated with these OCT imaging improvements is a reduced imaging depth. Imaging penetration within the vessel wall is limited to 1.5 mm and confines tissue characterization to the region of plaque most likely to rupture and thrombosis. We have previously described the impact of penetration depth on biomechanical characterization.[4]

In this paper, we build on our recent advances in optical coherence elastography (OCE)[3] by combining robust estimates of tissue velocity fields with vascular elastic modulus

---

Address correspondence to Dr. Mohammad Kaazempur Mofrad, Department of Bioengineering, University of California, Berkeley, 483 Evans Hall #1762, Berkeley, CA 94720. Electronic mail: mofrad@berkeley.edu
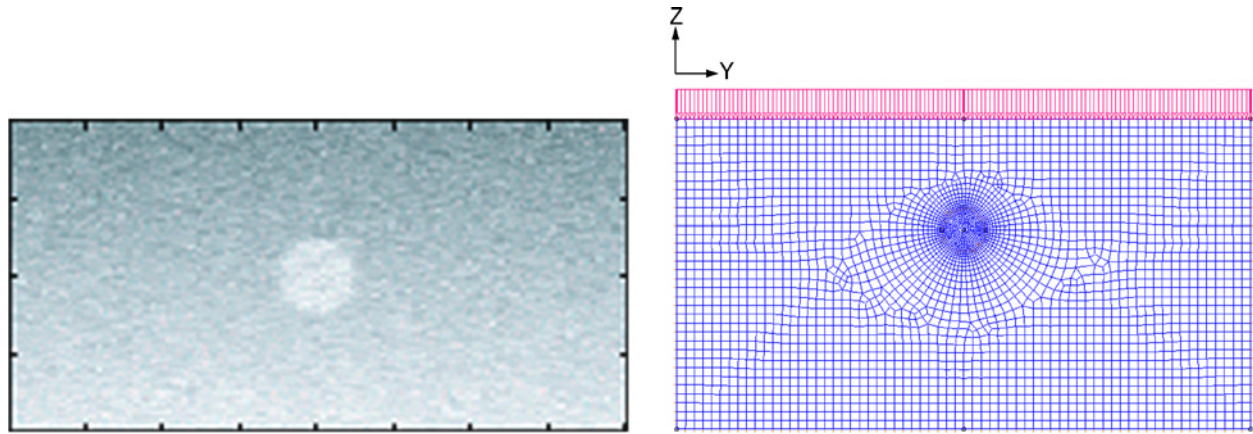
FIGURE 1. OCT image simulation of an inclusion within a tissue block (*left*) and its corresponding full FE model, consisting of 3163 elements (*right*). The technique for developing OCT image simulations based on tissue models has been previously described.[2] A displacement load was imposed on the tissue block model and image simulation.

estimation. We present a linear perturbation Gauss–Newton method for high-resolution modulus estimation and demonstrate results from simulated tissue compression imaging with time-domain OCE. High-resolution quantification of vulnerable atherosclerotic plaque material properties would allow the study of (i) the spatial distribution and magnitude of stress concentrations, which have been shown to correspond with regions where plaque rupture tends to occur,[24] and (ii) the relationship between mechanical stresses on vascular cells and features of vascular remodeling associated with atherogenesis.

METHODS

OCT Imaging and Elastography

Our methods for time-domain OCT imaging[2,17,28] and robust estimation of tissue velocity and strain fields have been described previously.[3] Robust velocity estimation is accomplished by minimizing a variational energy functional that contains side constraint terms, reflecting our prior knowledge about tissue biomechanical behavior:

$$\hat{v}(x, y) = \arg\min_v \{G(v(x, y))\} = \arg\min_v \{aG_D(v(x, y)) + cG_S(v(x, y)) + cG_I(v(x, y))\} \quad (1)$$

In this expression the estimated velocity field $\hat{v}(x, y)$, which is essentially analogous to a displacement field, minimizes the weighted combination of three energy functions. The first, G_D, controls data fidelity, whereby minimizing this term corresponds to simple cross-correlation coefficient maximization. The second term, G_S, imposes strain field smoothness, while the final term, G_I, exploits prior knowledge that biological tissues are typically assumed incompressible in the range of time scales relevant to elastography. These terms together penalize velocity field estimates that stray from these biomechanical conditions.

With previously described techniques,[3] OCT images of tissue blocks containing circular inclusions under uniaxial compression were simulated (Fig. 1). In short, we generated interference images by applying an exponential decay term to the convolution between the coherent OCT point spread function and the backscattering field. The distribution of backscattering arises from the point scattering inherent to a specimen's morphological structure. In order to replicate OCT backscattering fields commonly seen for arterial tissue and inclusions (i.e., higher mean backscattering in tissue relative to inclusion), we assigned backscattering values at discrete points by selecting independent uniform random variables with an empirically chosen variance of 10 for scatterers within the tissue block and of 2 for scatterers within the inclusion. Finally, the individual tissue scatterers were displaced using displacement fields from finite element modeling (FEM) of the tissue block, where a 0.15 mm displacement load was applied to the top surface over five timesteps.

Axial (z-direction) velocity results using the above-described variational energy technique were generated for a series of simulated tissue blocks, where the size of the inclusion and the elasticity modulus ratio (defined as $E_{\text{inclusion}}/E_{\text{background}}$) were varied (Fig. 2). Specifically, we varied the inclusion diameter within the morphologically accurate range of lipid pool and calcified nodule sizes and the modulus ratio between two values, 5 for calcification and 0.5 for lipid pool. This resulted in four models: (a) 0.5 mm diameter calcified nodule, (b) 0.5 mm diameter lipid pool, (c) 0.75 mm diameter calcified nodule, and (d) 0.15 mm diameter calcified nodule.

Gauss–Newton Method for Elasticity Estimation

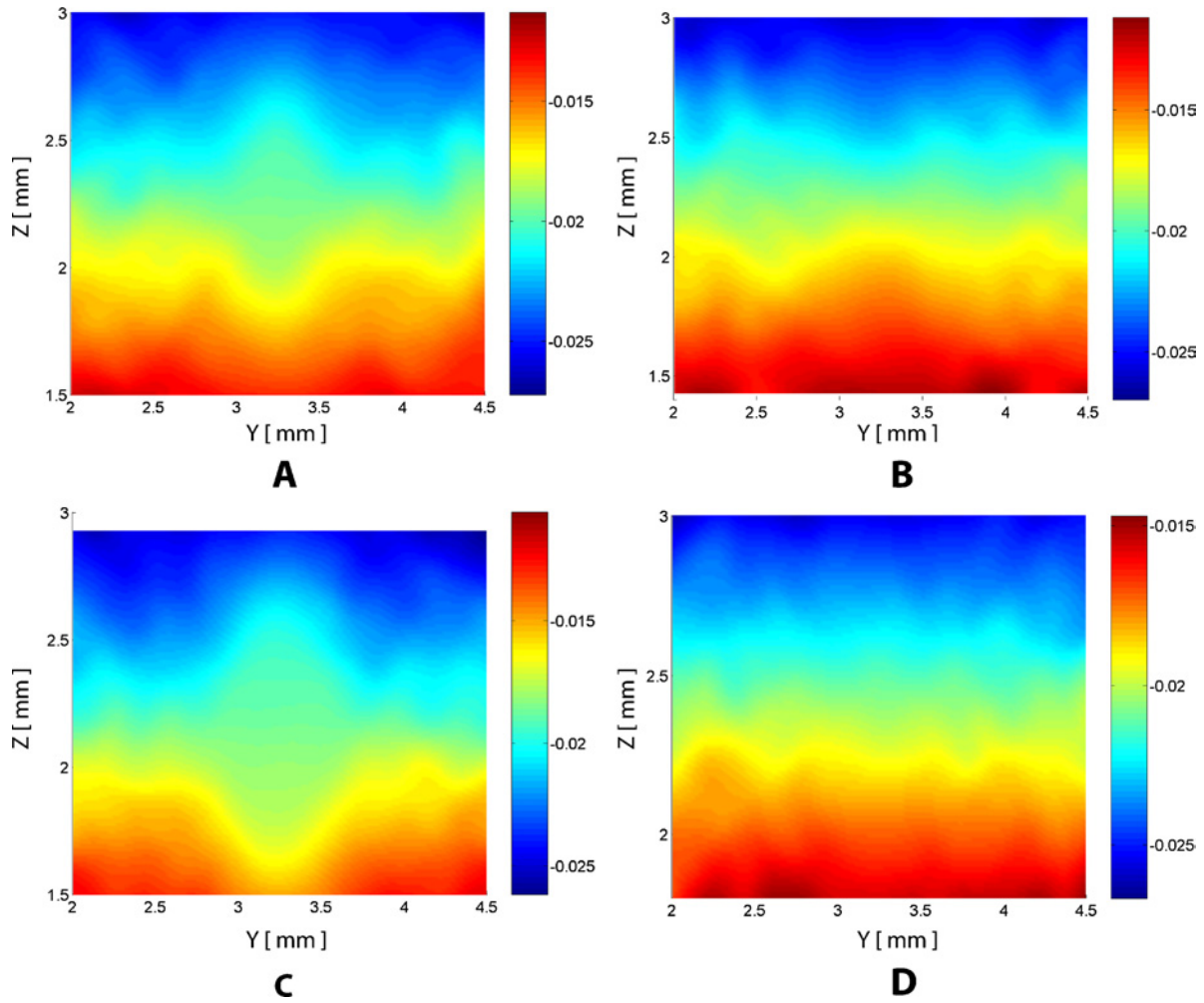Progress has been made to more accurately depict biological tissue in the form of constitutive models.

FIGURE 2. Axial (*z*-direction) velocity distributions for four tissue block inclusion diameter/E_{ratio} combinations: (A) 0.5 mm/5, (B) 0.5 mm/0.5, (C) 0.75 mm/5, (D) 0.15 mm/5. Results, which correspond to displacements in mm, were generated via a multi-resolution, variational energy minimization technique designed for OCE.

Hyperelastic models, where strain energy functions are used to capture the nonlinear nature of the stress–strain curve at high strains, are the most commonly used. Fung *et al.*[13] proposed an exponential type and it has since been applied to a wide array of tissue and modified to more truthfully mimic experimental data, for instance, in work by Holzapfel *et al.*[15,16] to describe the "biphasic" circumferential stress–strain relationship of arteries and to develop the full constitutive relations for the mechanical response of elastic arteries. Within the realm of elasticity estimation, however, researchers depend on the simpler, more direct linear elastic, isotropic model for two main reasons. First, elasticity estimation is a discrete, numerical effort, where elasticity values are assigned to individual elements based on displacement maps generated via image processing. As is evidenced by the description of the algorithm design (see below), fitting more than a single parameter to each element is not merely computationally rigorous but can be unattainable depending on the number of measured displacement data. Second, unlike a more traditional nonlinear constitutive model, elasticity estimation provides a comprehensive map of material properties, albeit Young's modulus values. Researchers continue therefore to rely on the linear elastic, isotropic model for elasticity estimation,[1,25] so long as the limits of the results of such estimation are understood as a way to probe the elasticity of specimens under small, quasi-static deformations.

Consider a body being displaced and that each point on the boundary of the solid is specified either by a stress or displacement. Let $v(x, y, z)$ denote its displacement field as a function of spatial coordinates x, y, z. The ensuing constitutive stress–strain relationship, assuming an incompressible, linear elastic solid is

$$\sigma_{ij} = -p\delta_{ij} + 2\mu\varepsilon_{ij}, \tag{2}$$

where σ_{ij} is a component of the stress tensor, μ is the material shear modulus, p is the pressure or hydrostatic stress, and δ_{ij} is the Kronecker delta. We write this relationship

in terms of an unknown shear modulus for convenience, where later it can simply be related to the Young's modulus and Poisson's ratio. Balancing linear momentum over each part of the material gives the equilibrium equations,

$$\frac{\partial \sigma_{ij}}{\partial x_j} + f_j = 0, \qquad (3)$$

where f_j, the body force per unit volume, is typically negligible. Because images are traditionally obtained in two-dimensional cross-sections, we simplify the system by invoking the plane strain approximation. The result, after combining Eqs. (2) and (3) under the plane strain approximation, is the "plane strain inversion equation"[27] for the single unknown shear modulus, μ:

$$\frac{\partial^2 (\varepsilon_{xy}\mu)}{\partial y^2} - \frac{\partial^2 (\varepsilon_{xy}\mu)}{\partial x^2} + 2\frac{\partial^2 (\varepsilon_{xx}\mu)}{\partial x \partial y} = 0. \qquad (4)$$

The derivation of the "plane strain inversion equation" was presented to give the reader a formulaic understanding of the problem, however, generally direct inversion for the shear modulus is avoided for various reasons. First, solutions are difficult to stabilize. Second, as shown in Eq. (4), direct inversion requires explicit knowledge of the strain field, which consequently demands differentiating an already noisy measured displacement field. Third, Eq. (4) insists on μ being twice differentiable, thus placing continuity restrictions on the modulus distribution and not allowing jump changes in its value. Instead, the preferred strategy for material property estimation is iterative inversion, where a nonlinear least squares (NLS) problem is formulated by attempting to minimize the difference between computed and measured mechanical responses (i.e., displacement fields).

The resulting system, known as the Inverse Problem (IP) in elastography, is written as

$$\text{Given} \quad v_c : R^p \to R^q, \quad q \geq p, \quad \text{solve}$$

$$\min_{E \in R^p} \left\{ \Phi(E) = \frac{1}{2} \|v_c(E) - v_m\|^2 \right\}, \qquad (5)$$

where E is the Young's modulus distribution, typically a one-dimensional vector ($p = 1$) if concerned with an *isotropic* distribution, $v_c(E)$ is the vector of computed displacements based on a given E, and v_m is the vector of measured displacements, after scaling the OCE estimated velocity results by the pixel sizes. We write the IP in terms of the unknown distribution E because we are most interested in inferring a direct elasticity measure, however, it can be written with equal correctness in terms of the shear modulus, as in the "plane strain inversion equation" derivation. It should also be noted that displacement fields lie in one-, two-, or three-dimensional space depending on the number of displacement components provided by elastography experiments. In most cases, including our two-dimensional experiments, we have axial (z) and lateral (y) displacements to compare.

In practice, we solve the inverse problem via a gradient-based numerical algorithm, where the residual (given in Eq. (5)) acts as the driving force. Kallel and Bertrand[19] proposed a linear perturbation Gauss–Newton method. By perturbing the elasticity distribution a "sufficiently" small amount, a gradient (or Jacobian) matrix can be constructed with the subsequent, observed perturbations in displacement and then used to direct the search toward the stationary point E^*. However, before arriving at a Newton update equation for the modulus distribution, we write expressions for the gradient and Hessian of $\Phi(E)$, the natural tools for locating the zero gradient minima criteria:

$$\nabla \Phi(E) = J (v_c(E))^T (v_c(E) - v_m) = J_v^T (v_c(E) - v_m), \qquad (6)$$

where J_v is the Jacobian of $v_c(E)$ with respect to E, and

$$\nabla^2 \Phi(E) = J_v^T J_v + \frac{\partial J_{vi}}{\partial E_j}(E) [I \otimes (v_c(E) - v_m)], \quad (7)$$

where I is the identity matrix and $\otimes$ is the Kronecker delta. In accordance with common practice, we neglect the second-order term in Eq. (7) based on the observation that it is typically small relative to the first-order term and is computationally expensive to calculate,[29] yielding the relationship

$$\nabla^2 \Phi(E) \approx J_v^T J_v. \qquad (8)$$

This Hessian simplification is a distinguishing characteristic of the Gauss–Newton method from other Newton's methods, and we elaborate on the ensuing limitations in the following section; however, suffice it to say the reduction yields a *symmetric* and *positive-definite* Hessian, so long as J_v is not singular, and thus a more solvable system.

Based on the above-mentioned strategy and assumptions, the final Newton update equation for the root direction of elastic modulus becomes

$$\Delta E = -\left[\nabla^2 \Phi(E)\right]^{-1} \nabla \Phi(E)$$

$$= -\left[J_v^T J_v\right]^{-1} \left[J_v^T (v_c(E) - v_m)\right]_k \qquad (9)$$

As already noted, we approximate the Jacobian with the displacement information gathered by discretely perturbing the elasticity distribution because an explicit expression for $v_c(E)$ is not easily known. Mathematically, this is a linear perturbation written in finite difference scheme: suppose we have a function $F(x) = (f_1, \ldots, f_n)^T$, then,

$$J(x)_{ij} = \frac{\partial f_i}{\partial x_j}(x) \approx \frac{f_i(x_j + \varepsilon|x_j|e_j) - f_i(x_j)}{\varepsilon|x_j|} \qquad (10)$$

for "sufficiently" small perturbation ε, where e_j is the unit basis vector in the jth direction.
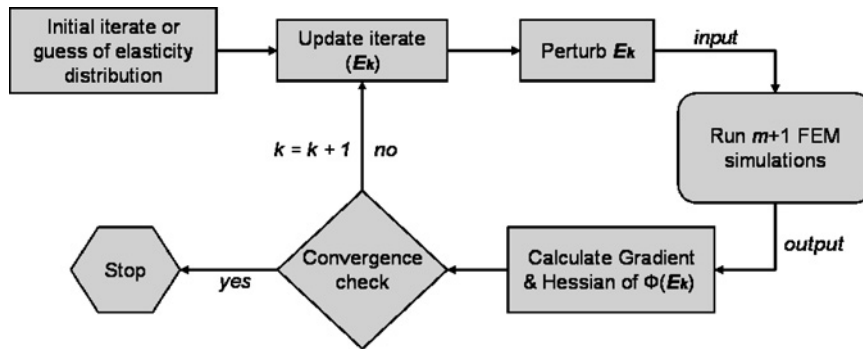
FIGURE 3. Flowchart of a Gauss–Newton method-based reconstruction algorithm. With an initial guess of the elasticity distribution, the algorithm estimates the gradients necessary to direct it to a solution by perturbing elasticity distributions.

Regularization Scheme

Inverse problems, especially when in the presence of noisy data, often yield ill-posed systems, thus requiring regularization schemes to stabilize and identify unique solutions. As a result, we equipped Eq. (5) with a Tikhonov regularization term, so that the objective of the Gauss–Newton method is not only to minimize the original data fidelity term but a linear combination of it and a modulus distribution smoothing term. The discrete system of equations making up the IP now become

$$\text{Given} \quad v_c : R^p \to R^q, \quad q \geq p, \quad \text{solve}$$

$$\min_{E \in R^p} \left\{ \Phi(E) = \frac{1}{2} \left\| v_c(E) - v_m \right\|_2^2 + \frac{\lambda}{2} \left\| LE \right\|_2^2 \right\}, \quad (11)$$

where λ is a weighting factor and $\|LE\|_2^2$ is the regularization term and a function of the regularized solution, E. This latter term is sometimes referred to as the *discrete smoothing norm* because the matrix L usually acts as a smoothing operator on the solution field.[14] Choice of L depends on the desired smoothing effect and includes, but is not exclusive to, identity matrices, weighted diagonal matrices, and discrete approximations for derivative and Laplacian operators.

Without going into extraneous detail, it should be noted that inclusion of a Tikhonov regularization term serves to augment the diagonal terms of the Hessian matrix ($J_v^T J_v$) via addition by the positive-definite, symmetric matrix $L^T L$. Recall that an ill-conditioned Hessian, one that is riddled with clusters of small singular values making its columns numerically linearly dependent, is the root of an ill-posed problem because, as Eq. (9) illustrates, it is the term being inverted. Hence, we can infer that boosting the diagonal of the Hessian also boosts its small singular values, thus producing a more well-posed system. This is especially important for IPs of this genre where the Hessian is abridged. Additionally, that second-order term shown in Eq. (7), which is neglected, becomes increasingly important as one deviates farther from the solution, and this is a primary reason why

many are so concerned with keeping initial guesses as close as possible to the actual solution.

Algorithm Design

A commercially available finite element software package ADINA (Watertown, MA) was employed to solve for the model displacements based on prescribed initial displacements, boundary conditions, model geometry, and material properties. In addition, an all-inclusive software program, tailored to automatically interface with ADINA, linearly interpolate and mesh OCT data with FEM data, and perform the iterative modulus estimation was developed. A detailed view of the modulus estimation (Gauss–Newton) algorithm is depicted in flowchart form (Fig. 3).

Model Description

Based on the four OCT models of varied inclusion diameter/E_{ratio} combination and their corresponding OCE velocity results, elasticity reconstruction distributions were generated. First, full FE models of the soft tissue rectangular blocks were generated (as shown in Fig. 1). All models satisfy the equilibrium equations for incompressible, linear elastic solids undergoing small, quasi-static deformations and the plane strain assumption. The models were meshed with nine-node quadrilateral elements and, for each discrete element, a Young's modulus (E) and Poisson's ratio ($\nu = 0.499$) were assigned. Next, in order to alleviate the computational intensity of the problem, we reduced the number of unknown elasticity values by coarsening the meshes of the full FE models, taking care of course not to jeopardize the high resolution capability of OCT. Specifically, the full finite element model (shown in Fig. 1) is composed of 12,855 global nodes and 3163 elements, far too many for making estimation a reasonable endeavor and unnecessary for making biomechanical conclusions. Additionally, OCE velocity results were generated for only a central subsection of the full FE model, i.e., the region of interest. This explains why the axes of the velocity distribution results (Fig. 2) do not begin at 0 and do not span the
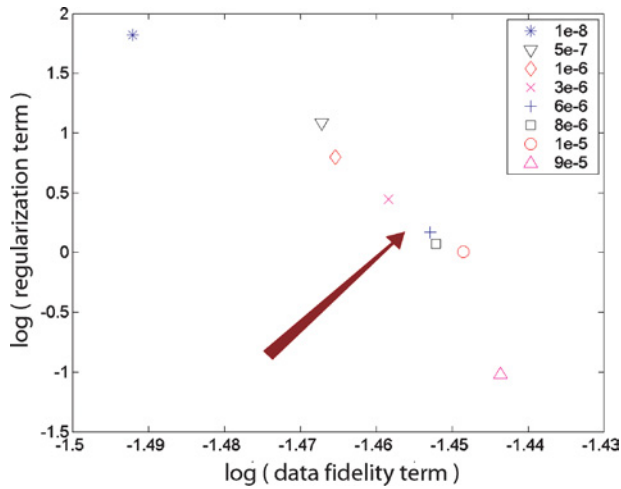
FIGURE 4. The *L*-curve result for $E_{ratio} = 5$ and 0.5 mm inclusion when log (data fidelity term) is plotted against log (regularization term). The plot indicates that data fidelity and regularization are optimally balanced when λ lies between 4×10^{-6} and 7×10^{-6} (*arrow*).

length of the full model. As a result of these two details, we were left with a smaller and more manageable subset of unknowns, from the full 3163 elements to 200 elasticity unknowns for the 0.5 mm inclusion, 262 unknowns for the 0.75 mm inclusion, and 203 unknowns for the 0.15 mm inclusion.

Based on these working finite element models, nodal displacement values were calculated and subsequently interpolated onto the OCT image grid in order to compare with the measured OCE velocity data. Then, in order to compute $\Phi(E)$, the OCE velocities, which were obtained in pixel sizes, were corrected via OCT resolution to give the realistic displacement measurements of the specimen under investigation. Axial (*z*-direction) and lateral (*y*-direction) pixel sizes for our OCT images were 1 μm and 25 μm, respectively.

In summary, while the unknown elasticity values remained in the finite element model grid, the displacements were mapped onto the OCT image grid. This is not surprising because while the FE models govern the number of unknowns in the problem, the solution is always limited by the number of measured data points, in this case, the OCE velocity results.

RESULTS

Empirical L-curve

Our first task was to optimize the regularization weighting factor in order to properly balance data fidelity and smoothing effects. We chose to solve this nontrivial problem empirically by constructing an *L*-curve, a log–log plot of the data fidelity term versus the smoothing term. For the regularization matrix *L*, we constructed piece-wise,

first-order derivative operators, applied to the elements of each region (background and inclusion) distinctly. The high soft tissue contrast, evident from the OCT images (Fig. 1), indicated a change in the tissue type between background and inclusion. This allowed us to qualitatively decouple the material regions and implicitly build material boundaries within the regularization matrix. With other imaging modalities that lack *a priori* tissue material discernment, this would be relatively difficult. Instead, smoothing operators would be applied over either the entire model or speculated regions of different tissue, thus most likely requiring more iterations or several attempts at the elasticity distribution before converging on an accurate solution.

According to the *L*-curve selection criterion, λ is the value that maximizes the curvature of this typically *L*-shaped curve. We found the ideal range of λ for a model with $E_{ratio} = 5$ and a 0.5 mm inclusion between 4×10^{-6} and 7×10^{-6} based on this empirical method (Fig. 4). Values of this magnitude confirm the presence of noise in the velocity data, as predicted; noise-free, or essentially noise-free, data would yield much smaller values of λ in order to grant more fidelity to the data.

Modulus Distribution Results

OCE results for four different tissue models were obtained (Table 1), and their corresponding modulus distributions were estimated via our Gauss–Newton method-based software. Elasticity estimates were accurate and smooth (Fig. 5). Furthermore, the corresponding displacement errors (between target and calculated displacement fields) confirmed convergence, as their values were more than 3 orders of magnitude less than the smallest model displacements.

Elasticity maps from previous estimation work[10,19] showed somewhat limited ability to resolve tissue inclusions on the order of 1–2 cm in size based on radio frequency (RF) ultrasonic echo elastography images. Here, with OCT elastograms, we demonstrate successful estimation on a myriad of examples, notably of inclusion diameters ranging from 0.75 mm to as small as 0.15 mm.

TABLE 1. Summary of the four elasticity models, corresponding estimate errors, and required iteration numbers. The estimate errors are root mean squared displacement errors normalized by the number of displacement data points in the OCT image grid, calculated as RMS error = $\frac{1}{N}\sqrt{\sum_{i}^{N}|v_c - v_m|_i^2}$.

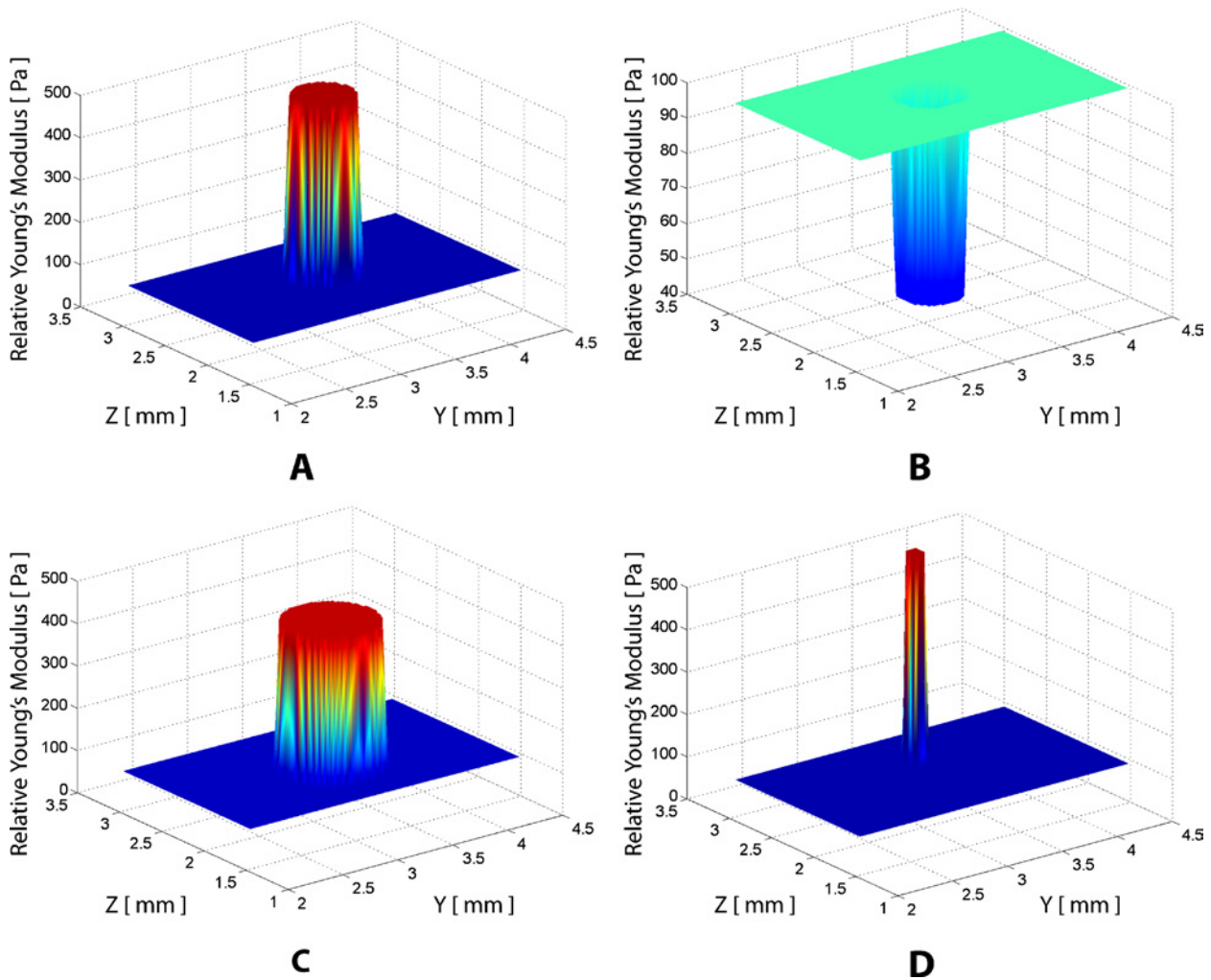| Model	Inclusion diameter (mm)	E_{ratio}	RMS error (mm)	Iterations
A	0.5	5.0	2.16×10^{-6}	10
B	0.5	0.5	2.24×10^{-6}	15
C	0.75	5.0	1.89×10^{-6}	10
D	0.15	5.0	2.30×10^{-6}	19

FIGURE 5. Elastic modulus distribution results for the following tissue block inclusion diameter/E_{ratio} combinations: (A) 0.5 mm/5, (B) 0.5 mm/0.5, (C) 0.75 mm/5, (D) 0.15 mm/5. Estimates were generated by applying the Gauss–Newton method software to corresponding OCE velocity estimates. The modulus results in all four cases corresponded to minimal errors in target vs. converged displacement fields. Converged results for all three models that reflect tissue blocks incorporating different sized calcified nodules (Models (A), (C), (D)) confirmed inclusion modulus values of approximately 500 Pa, while the results for Model (B), the sole simulation involving lipid pool, confirmed a lower modulus value than background (∼50 Pa).

Finally, an initialization experiment was done where the initial elasticity "guesses" were varied up to 100% of the approximate target values. The resulting convergence curves showed parallel and typical trends in the reduction of the displacement residual, indicating that accurate convergent estimates were not very dependent on the initial guess, yet, as expected, speed of convergence could be accelerated with a close initial value (Fig. 6).

CONCLUSIONS

The elasticity maps generated via OCT elastograms show promise for material property estimation of soft tissue and, in particular, of small length scale biological structures such as atherosclerotic plaques. This example is of great interest because of the strong dependence of

critical cardiovascular events on the biomechanical state of plaques. Plaque rupture was postulated and later confirmed to be a nearly essential precursor to cardiac events, such as infarction.[6,8] Furthermore, high circumferential stress concentrations within plaques were found to correspond to fissure prone regions.[5,24] Therefore, the ability to quantify vulnerable plaque materials, such as those of thin fibrous caps partitioning large, compliant lipid pools from vessel lumens, would be medically beneficial.

OCT is an invasive imaging technique with high spatial resolution and thus the ability to visualize structures on the size scale of thin fibrous caps. As a result, it is well suited as a scaffold for *in vivo* tissue elasticity estimation. In previous work,[10,19] elasticity estimates based on traditional imaging modalities have been limited by spatial resolution. In this work, we have developed a fully integrated system based on
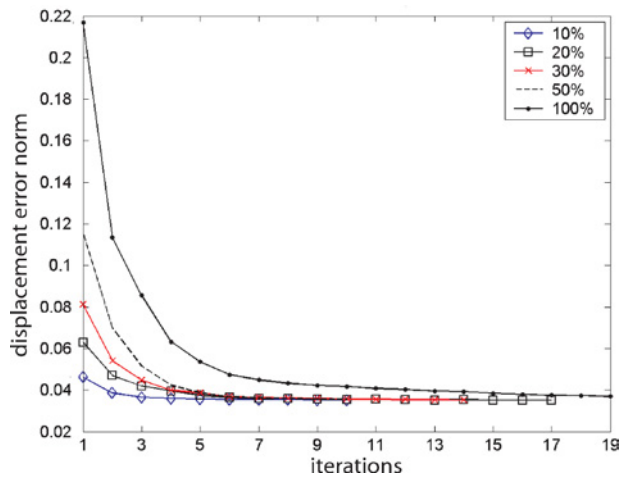
FIGURE 6. By varying the initial values of elasticity inputted into the algorithm and tracking the root mean squared displacement error, the robustness of the data and algorithm can be assessed. Constant elasticity values, differing by an increasing amount from the target distribution, were used to initialize the estimation algorithm. Typical convergence patterns and well-conditioned behavior were observed for initial values up to ±100% of the target modulus values.

OCT imaging, generated simulated soft tissue elastograms for a variety of tissue block with inclusion examples, and finally estimated corresponding elasticity fields. This is an important step toward gaining quantitative elasticity information from, for instance, *in vivo* OCT images of coronary arteries (Fig. 7). The results suggest a promising future for OCT-based material property estimation, with converged displacement residuals on the order of 10^{-6} mm, or more
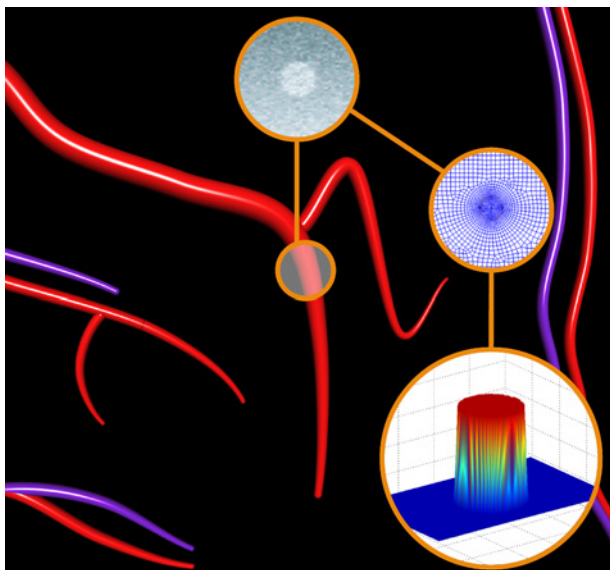

FIGURE 7. A rendering of a coronary artery network, where the insets signify various components of our OCT-based elasticity reconstruction method: From static *in vivo* OCT images to FE models and finally to the estimated elasticity distributions.

than 3 orders of magnitude less than average calculated displacements, and the ability to resolve the elasticity of very fine structures.

Future work includes quantifying the effects of image-based boundary condition and other parameter uncertainties on the elasticity results. Additionally, in the course of developing an OCT-based system for *in vivo* soft tissue characterization, we are currently obtaining velocity and elasticity estimates of *ex vivo* tissue specimens, in particular of aortic tissue.

REFERENCES

[1]Baldewsing, R. A., C. L. de Korte, J. A. Schaar, F. Mastik, and A. F. W. van der Steen. Finite element modeling and intravascular ultrasound elastography of vulnerable plaques: Parameter variation. *Ultrasonics* 42:723–729, 2004.

[2]Bouma, B. E., and G. J. Tearney. Power-efficient nonreciprocal interferometer and linear-scanning fiber-optic catheter for optical coherence tomography. *Opt. Lett.* 24:531–533, 1999.

[3]Chan, R. C., A. H. Chau, W. C. Karl, S. Nadkarni, A. S. Khalil, N. Iftimia, M. Shishkov, G. J. Tearney, M. R. Kaazempur-Mofrad, and B. E. Bouma. OCT-based arterial elastography: Robust estimation exploiting tissue biomechanics. *Opt. Express* 12:4558–4572, 2004.

[4]Chau, A. H., R. C. Chan, M. Shishkov, B. MacNeill, N. Iftima, G. J. Tearney, R. D. Kamm, B. E. Bouma, and M. R. Kaazempur-Mofrad. Mechanical analysis of atherosclerotic plaques based on optical coherence tomography. *Ann. Biomed. Eng.* 32:1494–1503, 2004.

[5]Cheng, G. C., H. M. Loree, R. D. Kamm, M. C. Fishbein, and R. T. Lee. Distribution of circumferential stress in ruptured and stable atherosclerotic lesions. A structural analysis with histopathological correlation. *Circulation* 87:1179–1187, 1993.

[6]Constantinides, P. Plaque fissure in human coronary thrombosis. *J. Atheroscler. Res.* 6:1–17, 1966.

[7]Costa, K. D., J. W. Holmes, and A. D. McCulloch. Modeling cardiac mechanical properties in three dimensions. *Philos. Trans. R. Soc. Lond. A.* 359:1233–1250, 2001.

[8]Davies, M. J., and T. Thomas. The pathological basis and microanatomy of occlusive thrombus formation in human coronary arteries. *Philos. Trans. R. Soc. Lond. B. Biol. Sci.* 294:225–229, 1981.

[9]de Korte, C. L., A. F. W. van der Steen, E. I. Céspedes, G. Pasterkamp, S. G. Carlier, F. Mastik, A. H. Schoneveld, P. W. Serruys, and N. Bom. Characterization of plaque components and vulnerability with intravascular ultrasound elastography. *Phys. Med. Biol.* 45:1465–1475, 2000.

[10]Doyley, M. M., P. M. Meaney, and J. C. Bamber. Evaluation of an iterative reconstruction method for quantitative elastography. *Phys. Med. Biol.* 45:1521–1540, 2000.

[11]Doyley, M. M., F. Mastik, C. L. de Korte, S. G. Carlier, E. I. Céspedes, P. W. Serruys, N. Bom, and A. F. W. van der Steen. Advancing intravascular ultrasonic palpation toward clinical applications. *Ultrasound Med. Biol.* 27:1471–1480, 2001.

[12] Duck, F. A. Physical Properties of Tissues—A Comprehensive Reference Book. Sheffield, UK: Academic Press, 1990.

[13] Fung, Y. C., K. Fronek, and P. Patitucci. Pseudoelasticity of arteries and the choice of its mathematical expression. *Am. Physiol. Soc.* 237:H620–H631, 1979.

[14] Hansen, P. C. Rank-Deficient and Discrete Ill-Posed Problems: Numerical Aspects of Linear Inversion. Philadelphia, PA: SIAM, 1998.

[15] Holzapfel, G. A., R. Eberlein, P. Wriggers, and H. W. Weizsäcker. Large strain analysis of soft biological and rubber-like membranes: Formulation and finite element analysis. *Comput. Methods Appl. Mech. Eng.* 132:45–61, 1996.

[16] Holzapfel, G. A., T. C. Gasser, and R. W. Ogden. Comparison of a multi-layer structural model for arterial walls with a fung-type model, and issues of material stability. *J. Biomech. Eng.* 126:264–275, 2004.

[17] Huang, D., E. A. Swanson, C. P. Lin, J. S. Schuman, W. G. Stinson, W. Chang, M. R. Hee, T. Flotte, K. Gregory, C. A. Puliafito, *et al.* Optical coherence tomography. *Science* 254:1178–1181, 1991.

[18] Jang, I. K., B. E. Bouma, D. H. Kang, S. J. Park, S. W. Park, K. B. Seung, K. B. Choi, M. Shishkov, K. Schlendorf, E. Pomerantsev, S. L. Houser, H. T. Aretz, and G. J. Tearney. Visualization of coronary atherosclerotic plaques in patients using optical coherence tomography: Comparison with intravascular ultrasound. *J. Am. Coll. Cardiol.* 39:604–609, 2002.

[19] Kallel, F., and M. Bertrand. Tissue elasticity reconstruction using linear perturbation method. *IEEE Trans. Med. Imaging* 15:299–313, 1996.

[20] Mow, V. C., S. C. Kuei, W. M. Lai, and C. G. Armstron. Biphasic creep and relaxation of articular cartilage in compression: Theory and experiments. *J. Biomech. Eng.* 102:73–84, 1980.

[21] Oomens, C. W. J., D. H. Campen, and H. J. vanGrootenboer. A mixture approach to the mechanics of skin. *J. Biomech.* 20:877–885, 1987.

[22] Ophir, J., E. I. Céspedes, H. Ponnekanti, Y. Yazdi, and X. Li. Elastography: A quantitative method for imaging the elasticity in biological tissues. *Ultrason. Imaging* 13:111–134, 1991.

[23] Ophir, J., E. I. Céspedes, B. Garra, H. Ponnekanti, Y. Huang, and N. Maklad. Elastography: Ultrasonic imaging of tissue strain and elastic modulus *in vivo*. *Eur. J. Ultrasound* 3:49–70, 1996.

[24] Richardson, P. D., M. J. Davies, and G. V. R. Born. Influence of plaque configuration and stress distribution on fissuring of coronary atherosclerotic plaques. *Lancet* 8669:941–944, 1989.

[25] Samani, A., J. Bishop, C. Luginbuhl, and D. B. Plewes. Measuring the elastic modulus of *ex vivo* small tissue samples. *Phys. Med. Biol.* 48:2183–2198, 2003.

[26] Schaar, J. A., C. L. de Korte, F. Mastik, C. Strijder, G. Pasterkamp, E. Boersma, P. W. Serruys, and A. F. W. van der Steen. Characterizing vulnerable plaque features with intravascular elastography. *Circulation* 108:1–6, 2003.

[27] Skovoroda, A. R., S. Y. Emelianov, and M. O'Donnell. Reconstruction of tissue elasticity based on ultrasonic displacement and strain images. *IEEE Trans. Ultrason. Ferroelectr. Freq. Control* 42:747–765, 1995.

[28] Tearney, G. J., M. E. Brezinski, B. E. Bouma, S. A. Boppart, C. Pitris, J. F. Southern, and J. G. Fujimoto. *In vivo* endoscopic optical biopsy with optical coherence tomography. *Science* 276:2037–2039, 1997.

[29] Yorkey, T. J., J. G. Webster, and W. J. Tompkins. Comparing reconstruction algorithms for electrical impedance tomography. *IEEE Trans. Biomed. Eng.* 34:843–852, 1987.